RESEARCH ARTICLE - APPLICATION

WILEY

Computational model of silica nanoparticle penetration into tumor spheroids: Effects of methoxy and carboxy PEG surface functionalization and hyperthermia

Abhignyan Nagesetti[1] | George S. Dulikravich[2] | Helcio R. B. Orlande[3] |
Marcelo J. Colaco[3] | Anthony J. McGoron[1]

[1]Department of Biomedical Engineering, Florida International University, Miami, Florida, USA

[2]Department of Mechanical and Materials Engineering, Florida International University, Miami, Florida, USA

[3]Department of Mechanical Engineering, Federal University of Rio de Janeiro, Rio de Janeiro, Brazil

Correspondence
Anthony J. McGoron, Department of Biomedical Engineering, Florida International University, Miami, FL, USA.
Email: mcgorona@fiu.edu

Abstract

Drug delivery to tumors suffers from poor solubility, specificity, diffusion through the tumor micro-environment and nonoptimal interactions with components of the extracellular matrix and cell surface receptors. Nanoparticles and drug–polymer complexes address many of these problems. However, large size exasperates the problem of slow diffusion through the tumor. Three-dimensional tumor spheroids are good models to evaluate approaches to mitigate these difficulties and aid in design strategies to improve the delivery of drugs to treat cancer effectively. Diffusion of drug carriers is highly dependent on cell uptake rate parameters (association/dissociation) and temperature. Hyperthermia increases molecular transport and is known to act synergistically with chemotherapy to improve treatment. This study presents a new inverse estimation approach based on Bayesian probability for estimating nanoparticle cell uptake rates from experiments. The parameters were combined with a finite element computational model of nanoparticle transport under hyperthermia conditions to explore its effect on tumor porosity, diffusion and particle binding (association and dissociation) at cell surfaces. Carboxy-PEG-silane (cPEGSi) nanoparticles showed higher cell uptake compared to methoxy-PEG-silane (mPEGSi) nanoparticles. Simulations were consistent with experimental results from Skov-3 ovarian cancer spheroids. Amorphous silica (cPEGSi) nanoparticles (58 nm) concentrated at the periphery of the tumor spheroids at 37°C but mild hyperthermia (43°C) increased nanoparticle penetration. Thus, hyperthermia may enhance cancer treatment by improving blood delivery to tumors, enhancing extravasation and penetration into tumors, trigger release of drug from the carrier at the tumor site and possibly lead to synergistic anti-cancer activity with the drug.

KEYWORDS
chemotherapy, confocal microscopy, extracellular matrix, finite element modeling, Markov chain Monte Carlo, nanomedicine

1 | INTRODUCTION

1.1 | Macromolecule transport in tumor tissues

It is well accepted that despite the many (at least potential) advantages of nanoparticles as drug delivery vehicles, relatively few have advanced to clinical trials and fewer still to full regulatory approval. With the exceptions of liposomal formulations and Abraxane®, an albumin-bound paclitaxel, the use of nanoparticles for cancer has not served as the "silver bullet" predicted by many investigators. There are likely many reasons for this. The dependence of nanoparticle bio-distribution on particle size, shape, charge, and surface coatings has been extensively studied,[1–3] but remains inconclusive due to the variability in cancer biology. It is recognized that the environment in which the nanoparticles must travel before reaching its site of action is very complex and requires different nanoparticle physical characteristics at different parts of the journey (i.e., while in storage, reconstituted as an injectable form, in the plasma, crossing the capillary wall, transporting through the tumor interstitial space, crossing the cancer cell membrane, and finally in the intercellular space reaching its intended site of action). Much of the effort toward optimizing nanoparticles as drug delivery vehicles has concentrated on making the particles stealth while in the plasma, making them small so that they can easily pass through the capillary barrier, making them targeted so that they can recognize and enter the cancer cell, as well as the characteristics necessary for drug release and intracellular compartmentalization. Transport within the tumor extracellular matrix (ECM) is also important, but is less extensively studied.

In tumors with poorly developed vasculature, diffusion is the dominant mode of transport to deliver macromolecules into the tumor tissue.[4,5] Macromolecules of large size and high molecular weight have lower diffusion coefficients and hence diffuse slower than small size molecules. Dreher et al.[6] showed that dextrans of medium molecular weight (40–70 kDa) penetrated more efficiently into tumor tissue compared to dextrans of high size (3 MDa), providing an important drug carrier design criterion. In tumors, however, the diffusion coefficient is further dependent on the available fraction of fluid space (porosity) to diffuse and the binding affinity of macromolecules with tumor cells and extracellular components. Tumors with high packing density (low porosity) of cells offer more resistance to diffusion compared to tumors with low packing density (high porosity). Similarly, molecules with high binding affinity to tumor cells or components of the ECM diffuse slowly into the tissue. Presently, experimental estimation of rate constants requires expensive instrumentation (such as a flow cytometer or confocal microscope) and is subject to high variability. This proves to be a bottleneck for high throughput screening of nanoparticle properties for a chosen cancer cell type. Hence, a reliable estimation framework that can simulate cell uptake from simple experimental data is likely to speed up the development of personalized nanotherapies. One such inverse estimation approach to predict cell uptake rate constants from experimental data is presented in this work.

1.2 | Multicellular tumor spheroids

Small in vitro avascular multicellular tumors have been developed for drug screening and to track the transport of drug–polymer conjugates and nanoparticle drug carriers which can facilitate the evaluation of their efficacy.[7–10] Tumor spheroids are formed when cells aggregate and secrete ECM to give the cells structure in suspension. The formation of the ECM is typically promoted and enhanced with the addition of collagen, fibronectin, or commercial products such as Matrigel©, an undefined gelatinous mixture excreted by Engelbreth-Holm-Swarm (EHS) mouse sarcoma cells. Spheroids mimic many of the structural and functional features of a tumor microenvironment, such as a nutrients, oxygen, and pH gradient,[11–15] but importantly, not the presence of a vasculature. In addition to the ECM, spheroids may also generate functional cell-to-cell contacts such as E-cadherin junctions and tight gap junctions (desmosomes).[16] Drug transport data from tumor spheroids are particularly suitable to validate computational models of nanoparticle transport as presented in this article.

1.3 | Chemotherapy and hyperthermia

Cancer cells are more susceptible to mild hyperthermia than are normal cells and thus a strategy to reduce off-site toxicities and enhance the efficacy of chemotherapy is to combine chemotherapy with regional hypothermia.[17–19] In fact, according to a search of the ClinicalTrials.gov database there are 45 current (active, recruiting, or not yet recruiting)

phase 3 trials with the keywords Cancer AND Chemotherapy AND Hyperthermia and another 45 that are completed. Our own group has developed nanoparticles that combine chemotherapy with a thermo-responsive dye to induce mild hyperthermia.[20–23] We have found that, in uterine sarcoma cells, long duration slow-rate hyperthermia at 43°C induced mild cell apoptosis while, short duration fast rate hyperthermia causes necrosis.[21] Hyperthermia therapy and doxorubicin chemotherapy were found to be synergistic, or at least provide a more than the additive effect of the individual treatments. Slow-rate hyperthermia represents a scenario of whole organ or regional hyperthermia, while fast-rate hyperthermia represents a scenario of localized targeted hyperthermia. Lacking from the current literature is a detailed examination of the effects of hyperthermia on the transport of nanoparticle drug carriers through solid tumors. In the current study, the effect of long duration (slow rate) hyperthermia on silica nanoparticle transport into tumor spheroids is modeled. The Arrhenius formula was used to model the temperature dependence of solute-membrane reaction rates in a numerical model of nanoparticle transport. Further, the effects of hyperthermia on tumor porosity were modeled.

2 | MATHEMATICAL DESCRIPTION OF TRANSPORT IN TUMORS

The defined geometry of spheroids simplifies the mathematical representation of macromolecule transport toward identifying properties for optimal distribution. The advection–reaction (AR) model for studying penetration of antibodies, antibody fragments and free drug moieties has been reported.[24,25] Predictions of antibody transport from this model have been validated with experiments.[26] The basic mathematical framework presented below (Equation 1) is also applicable to model transport of moieties larger than antibodies, namely, nanoparticles.

$$\frac{\partial C}{\partial t} = \frac{1}{r^2} \frac{\partial}{\partial r} \left[D_{\text{eff}} \varepsilon r^2 \frac{\partial}{\partial r} \left(\frac{C}{\varepsilon} \right) \right] - k_{\text{a}} C_{\text{bs}} \frac{C}{\varepsilon} + k_{\text{d}} C_{\text{b}} \tag{1}$$

Equation (1) is the general form of Fick's second law of diffusion in spherical coordinates relating the rate of change of concentration C (M; molar concentration) in the spheroid with change of flux as a result of a concentration gradient. This rate is determined by the porosity (ε), effective diffusion coefficient (D_{eff}; m^2 s^{-1}), and a reaction component governed by association (k_{a}; M^{-1}/s) and dissociation (k_{d}; s^{-1}) rate constants. Porosity (ε) is a dimensionless variable that is defined as the fraction of void volume to total volume. For a porous medium (spheroid) immersed in liquid the void volume is filled with fluid and acts as a diffusing medium for macromolecules.[27,28] C_{bs} is the concentration of binding sites and C_{b} is the concentration of solute bound to the membrane. The ideal diffusion coefficient of a molecule (D_0) is determined from its size using the Stokes–Einstein relation. However, D_0 is not sufficient to describe molecule diffusion in porous media. D_0 is modified to the effective diffusion coefficient (D_{eff}) that accounts for available volume fraction for diffusion and hydrodynamic interactions between solutes and solid matrix (Equation 2).[28]

$$D_{\text{eff}} = D_0 \frac{L(\lambda)}{F \tau(\varepsilon)} \tag{2}$$

In Equation (2), λ is defined as the ratio of molecule to pore radius. As $\lambda \to 0$ solute pore interactions can be ignored. $L(\lambda)$ accounts for the hydrodynamic and steric reduction of diffusion in a pore. For $\lambda < 0.4$, $L(\lambda)$ is represented by Equation (3). In Equation (2), F is the shape factor, $\tau(\varepsilon)$ represents the tortuosity, that is, increased path length between two points in a porous medium that is measured by the distance between the points through connected pores (Equation 4).[28]

$$L(\lambda) = (1 - \lambda)^2 \left(1 - 2.1044\lambda + 2.089\lambda^3 - 0.984\lambda^5 \right) \tag{3}$$

$$\frac{1}{\tau(\varepsilon)} = 1 - \frac{2}{3}(1 + \varepsilon)(1 - \varepsilon)^{2/3} \tag{4}$$

Equations (2)–(4) describe the physical parameters that influence the transport of molecules in a porous medium. Additionally, solutes can bind to cell membranes and can also be internalized by the cells. Therefore, the total

concentration of solute in a spheroid is the sum of solute in the fluid phase (C), solute bound to cell membranes (C_b), and solute internalized by the cells (C_i) (Equation 5).

$$C_{tot} = C + C_b + C_i \tag{5}$$

It is assumed that cells do not migrate and that binding sites on cells are recycled at a constant rate. Hence, concentration of binding sites (C_{bs}) is solely dependent on the association and dissociation of solute on the cell membrane (Equation 6)

$$\frac{\partial C_{bs}}{\partial t} = -\frac{\partial C_b}{\partial t} = k_a C_{bs} C - k_d C_b - k_i C_b \tag{6}$$

The bound solute (C_b) is subsequently internalized by cells, exocytosis of solutes (*i.e.*, recycling back to the surface) can be neglected here as it is very slow compared to internalization and does not have any significant or direct contribution to the concentration flux. Rate of internationalization is determined by k_i as shown by Equation (7).

$$\frac{\partial C_i}{\partial t} = k_i C_b \tag{7}$$

Equations (1), (6), and (7) need to be solved simultaneously to obtain total concentration of a solute in the spheroid with the following initial and boundary conditions (I.C and B.C.)

$$\text{Initial conditions}: C(0,r) = (C_i(0,r) = C_b(0,r) = 0; C_{bs}(0,r) = \frac{2}{\pi} \frac{k_\beta \beta \varepsilon}{a^2 r_p N_A} \tag{8}$$

Dirichlet boundary condition: $C(t, R) = C_0$
Neumann boundary condition: $\frac{\partial C}{\partial r}(t,0) = 0$

The initial condition for C_{bs} is from Goodman *et al.*[29] and is dependent on porosity (ε), the available binding site fraction (β), the radius of the nanoparticle (a), the effective pore radius (r_p). The difference in the binding site density on cells in mono-layer culture compared to cells grown as spheroids, which experience more cell-to-cell interactions, is denoted by k_β. N_A is Avogadro's number. Values of physical parameters such as porosity for different tumor types are available from the literature or determined from spheroid cross sections using scanning electron or transmission electron microscopy. Particle radius is determined from scanning electron microscopy or through dynamic light scattering. Determination of the cell uptake rate constants (k_a, k_d, k_i) and binding sites require independent experiments since each cell type has different membrane and uptake properties.

2.1 | Mathematical models of cell uptake kinetics

The uptake of macromolecules by cells happens via passive diffusion or through energy dependent endocytosis. For macromolecules with size greater than 5 nm, endocytosis is the primary mode of uptake. Endocytosis happens via absorption of molecules on clathirin or caveolae coated pits on the cell membrane led by membrane invagination, wrapping and subsequent "pinching" of the clathirin/caveolae vesicles into the cell. The uptake of ligands targeted specifically to receptors on cells happens via receptor mediated endocytosis. Two different formulations have been widely used to model molecule uptake into cells; (1) based on adsorption kinetics (Langmuir kinetics) and (2) based on thermodynamics of membrane wrapping (energy formulation).

2.1.1 | Langmuir kinetics

Langmuir kinetics assumes the cell surface as a Langmuir membrane with finite capacity for binding molecules (N_0).[30] The number/mass of particles adsorbed at any time on the cell surface is proportional to the number of particles in the extracellular medium (N_{ext}) and the number of particles that can still bind to the cell surface ($N_0 - N(t)$). The

extracellular medium acts as a reservoir that is assumed to be a non-depleting source (constant) of molecules at the boundary of the tumor. This is a valid assumption since the number of molecules is very high compared to the number of cells at any time. The number of molecules desorbing from the surface is proportional to the absorbed molecules ($N(t)$). The proportionality constants are specified by association (k_a; $M^{-1} s^{-1}$) and dissociation (k_d; s^{-1}) rate constants. Therefore, the rate of change of the number of molecules on the cell surface is mathematically expressed by Equation (9)

$$\frac{dN(t)}{dt} = k_a N_{ext}(N_0 - N(t)) - k_d N(t) \tag{9}$$

A fraction of adsorbed particles is internalized at a rate k_i by the cells through endocytosis in Equation (10). The internalized particles are also actively recycled back to the cell membrane at an externalization rate, k_{rec}.

$$\frac{dN_i(t)}{dt} = k_i N(t) - k_{rec} N_i(t) \tag{10}$$

2.1.2 | Determination of cell uptake constants using Langmuir kinetics

The Langmuir kinetic model has been widely used to fit experimental data to estimate the rate constants of macromolecule uptake by cells. However, the model cannot be used directly to independently model $N(t)$ and $N_i(t)$ since this information is often not readily available from cell experiments. The information available on total cell concentration is the sum of $N(t)$ and $N_i(t)$. Therefore, additional experiments that make some *a priori* assumptions regarding cell uptake or specialized techniques are necessary to explicitly extract $N(t)$ and $N_i(t)$. Conventionally, to estimate membrane concentration, cells are incubated with solute of interest at 4°C where the internalization and externalization processes are assumed to be dormant (*i.e.*, k_i and $k_{rec} = 0$). The measured concentration is fitted to Equations (9) and (10) using a nonlinear least squares method (*e.g.*, Levenberg–Marquadt) to obtain k_a and k_d. The uptake experiments were repeated at 37°C and the information on k_a and k_d obtained at 4°C is used to estimate k_i and k_{rec}. It has been mentioned above that association and dissociation rate constants are strongly dependent on temperature and hence using k_a and k_d obtained at different temperatures will lead to an inaccurate representation of uptake kinetics. Furthermore, it has been shown that small nanoparticles enter cells even at 4°C via energy independent pathways.[31]

3 | INVERSE ESTIMATION OF UNKNOWN PARAMETER

If Equations (9) and (10) are treated as a direct, or forward problem, then the values of k_a, k_d, k_i, and k_{rec} are known and the differential equations can be solved, based on a set of initial conditions, to study the time evolution of cell uptake. Alternatively, an inverse formulation uses the information on $N_{tot}(t)$ available from experiments to recover the cell uptake parameters.[32–34] This set of parameters is denoted by a vector.

$$P^T = [P_1, P_2, ..., P_n] \tag{11}$$

In Equation (11), n is the number of parameters. The experimental measurement of response or output of a physical system is denoted in vector form by Equation (12).

$$N_{tot}^T = [N_{tot}^1, N_{tot}^2, ..., N_{tot}^3] \text{ where } N_{tot}^i = N_{tot}(t_i), i = 1, 2, ..., I. \tag{12}$$

One of the common approaches to solve an inverse problem is to estimate the parameter set P^T with a given set of experimental measurements $N_{tot}(t_i)$ by maximizing the likelihood probability density function (pdf) or by minimizing the exponent of likelihood pdf (Equation 13).[35,36]

$$\pi\left(N_{\text{tot}}^T \middle| P^T\right) = (2\pi)^{-1/2} |W|^{1/2} \exp\left\{-\frac{1}{2}[N_{\text{tot}} - V_M(P)]^T W^{-1}[N_{\text{tot}} - V_M(P)]\right\} \tag{13}$$

$V_M(P)$ is the set of responses generated by the system (forward problem) for a given set of P. The likelihood pdf specifies the relative probability of different measurement outcomes N_{tot} with a fixed P. Equation (13) is formulated on the assumption that measurement errors are Gaussian random variables with zero means and covariance matrix W. Furthermore, it is also assumed that the errors in measurements are independent of the parameters P. The likelihood pdf is based on the classic Bayesian statistics and is not dependent on the modeling of prior information regarding the system and related uncertainty about the unknown parameters.

Bayes theorem specifies the conditional probability of P occurring given a set of measurements N_{tot}. It serves as a mechanism to combine new information (experimental measurements) with previously available information (known as the prior). Furthermore, Bayes theorem is the basis of a statistical inversion approach based on the following principles; (1) all variables occurring in the inverse problem are considered random; (2) the randomness describes the degree of information related to their realization, which is coded into the likelihood pdf; (3) the solution of the inverse problem is recast in the form of statistical inference from the posterior probability density. Bayes theorem is mathematically stated as:

$$\pi_{\text{posterior}}(P) = \pi(P|N_{\text{tot}}) = \frac{\pi(P)\pi(N_{tot}|P)}{\pi(N_{tot})} \tag{14}$$

where $\pi_{\text{posterior}}(P)$ or $\pi(P|N_{\text{tot}})$ is the posterior distribution of parameters and is interpreted as the conditional probability of P occurring for a given set of measurements N_{tot}. $\pi(P)$ is the prior probability distribution of parameter set, $\pi(N_{\text{tot}}|P)$ is the likelihood function and $\pi(N_{\text{tot}})$ is the marginal probability of the measurements.

The application of Bayes theorem predicts the posterior distribution, which is sampled in this work using Markov chain Monte Carlo (MCMC) methods. The Metropolis–Hastings (MH) algorithm is the most widely used to implement the MCMC method.[37] The MH algorithm is implemented by choosing a sample distribution $p\left(P^*, P^{(t-1)}\right)$ which is used to draw a new candidate P^* given the sample at the current state of the Markov chain $P^{(t-1)}$. Once the proposal distribution is selected, the MH algorithm is repeated as follows:

1. Sample the proposal distribution based on the current state of the Markov chain.
2. Calculate the acceptance factor

$$\alpha = \min\left\{1, \frac{\pi\left(P^*|N_{\text{tot}}\right)p\left(P^{(t-1)}, P^*\right)}{\pi\left(P^{(t-1)}|N_{\text{tot}}\right)p\left(P^*, P^{(t-1)}\right)}\right\} \tag{15}$$

3. Generate a random variable U that is uniformly distributed on the interval 0 to 1.
4. If $U \le \alpha$, then set $P^{(t)} = P^*$, else set $P^{(t)} = P^{(t-1)}$.
5. Return to step 1 and repeat to generate samples $\{P^{(1)}, P^{(2)}, ..., P^{(i)}\}$ of the posterior distribution.

The above algorithm generates a sequence of the posterior distribution and the inference on this distribution is obtained from the inference on samples $\{P^{(1)}, P^{(2)}, ..., P^{(i)}\}$. However, a certain number of samples have to be discarded before the Markov chain reaches equilibrium (known as the burn-in period).

4 | METHODS FOR CELL AND SPHEROID NANOPARTICLE UPTAKE AND TRANSPORT

Inorganic nanoparticles made from silver, silica and gold offer advantages such as (1) control over size and surface properties, and (2) ease of loading with various fluorescent agents.[38] Silica nanoparticles were chosen for our studies since silver and gold nanoparticles without citrate stabilization more easily flocculate in physiological buffers and are not as stable against aggregation. Under typical clinical use conditions, silver and gold nanoparticles would be citrate

stabilized. Aggregation increases effective particle diameter and induces high experimental variability that is often difficult to model without explicit information on its dynamics. Moreover, silver particles induce cell toxicity due to leaching of silver ions in physiological buffers.

4.1 | Nanoparticle preparation

Fluorescent silica nanoparticles (~58 nm) were prepared by a slight modification of the reverse microemulsion method.[39] Briefly, 1.6 mg fluorescein isothiocyanate (FITC) was reacted with 20 μL 3-aminopropyltriethoxysilane (APTES) in 1 mL ethanol (200 proof) for 6 h. The ternary emulsion was prepared by adding 7.8 mL cyclohexane, 1.6 mL 1-hexanol (co-surfactant), 1.77 mL Triton X-100 (surfactant), 480 μL de-ionized water (18 MΩ), 100 μL of APTES-FITC mixture, and 100 μL tetraethylorthosilicate (TEOS) (silica precursor). The mixture was stirred on a rotor plate at 800 rpm for 30 min after which 65 μL of aqueous ammonia (28% in water) was added. The stirring was allowed to proceed under a nitrogen atmosphere for 48 h after which the nanoparticles were recovered by adding ethanol to the microemulsion. The recovered particles were washed 2 times with ethanol and 1 time with NaOH solution (8 mM) to get rid of the unentrapped dye (FITC) and the surfactant. The final yellow product (FITC-SiNP) was resuspended in 5 mL, 8 mM NaOH solution using sonication and was stored at 4°C until further use.

FITC-SiNP was modified with polyethylene glycol. Methoxy-PEG-silane (mPEGSi) or carboxy-PEG-silane (cPEGSi) was dissolved in water at 5 mg/mL and used for pegylation of the nanoparticle surface. Nanoparticle suspension (2.5 mL) was mixed with 10 mL DI water containing 50 μL aqueous ammonia and sonicated for 5 min. This was followed by the addition of 15 μL of TEOS and 1 mL of PEG solution. The mixture was vigorously stirred at 60°C for 15 h. The particles were washed three times using a 100 kDa centrifugation filter to get rid of unattached PEG. Finally, the particles were resuspended in 1 mL DI water and stored at 4°C for further experiments.

4.2 | Nanoparticle characterization

The size and surface charge were characterized using dynamic light scattering (DLS) (Malvern nano series Zetasizer). Silica content of nanoparticles was estimated using the blue molybdosilicic assay as per manufacturer's instructions. The number of silica nanoparticles was calculated by assuming a monodisperse size distribution and the known density value of silica, that is, 2.0 g cm^{-3}. A calibration curve of fluorescent intensity and number of silica particles was prepared by the measurement of fluorescence at $\lambda_{em} = 515$ nm's and $\lambda_{ex} = 480$ nm's by serial dilutions of FITC-SiNP. The calibration curve was linear within the measured limits of nanoparticle concentration.

4.3 | Cell uptake kinetics of nanoparticles

Skov-3 cells cultured under standard conditions were seeded in a 96 well plate at a density of 25,000 cells/well and allowed to attach overnight in an incubator. PEGylated-FITC loaded silica nanoparticles (PEGSiNp) modified with methoxy-PEG (mPEGSi) or carboxy-PEG (cPEGSi) were incubated with McCoy's 5A media for 30 min prior to addition to the cells at different concentrations (for determining dose dependent uptake) to determine the optimal concentration at which the cell uptake of nanoparticles saturated. The time kinetics of nanoparticle uptake was studied by incubating the cells with an optimal concentration (determined via dose dependent uptake study to be 100 μg/mL) of PEGSiNp nanoparticles at different time intervals. Every hour following the incubation (i.e., 1, 2, ..., 5 h), the cells in the wells were washed three times with ice-cold DPBS to get rid of free nanoparticles from the extracellular medium. The total nanoparticle concentration in the cells was determined from FITC fluorescence using a multi plate reader. Fluorescence intensity from FITC was corrected by subtracting the intensity obtained from cells without any PEGSiNp-loaded nanoparticles. After the completion of the uptake study, cell number was estimated using the SRB assay. The estimated protein content in each well was converted to cell number using a calibration curve of SRB protein content versus cell number.

The effect of hyperthermia (43°C) on cell uptake of PEGSiNp loaded silica nanoparticles was studied in a cell culture incubator. The cells were placed in the incubator set at 43°C and allowed to equilibrate for 50 min and followed by the addition of the PEGSiNp. The temperature of a well was monitored using a sterile thermocouple. Cells were

incubated with PEGSiNp at 43°C for 1 h, after which the plates were moved to a 37°C incubator. Nanoparticle uptake was determined in a similar manner as described above. FITC fluorescence was converted to the number of Si nanoparticles and divided by number of cells to estimate nanoparticle per cell.

4.4 | Spheroid generation

Hyperthermia was investigated to improve nanoparticle distribution in the tumor. Spheroids were created using the liquid overlay method[40,41] using Skov-3 human ovarian cancer cells in 96-well plates coated with agarose as described previously.[23] Cells in 2.5% (v/v) Matrigel© were added to wells of the 96-well plate. Spheroids were used 5 days after seeding at which time they were roughly round, compact and ~330 μm in diameter. Spheroids were characterized by histology and scanning electron microscopy (SEM) and viability using trypan blue assay. Additional details of the methods as well as results and discussion of structure and viability experiments can be found in our previous paper.[23]

To measure nanoparticle tumor penetration, spheroids were transferred to glass imaging dishes and incubated for 24 h with cPEGSi at 37°C or 43°C in a manner similar to monolayer cells described above. The mPEGSi nanoparticles were not tested due to low cell uptake. Prior to imaging, spheroids were treated with (4′,6-diamidino-2-phenylindole) (DAPI; nuclear stain) for 30 min followed by fixation with 4% formalin. The spheroids were mounted with Fluoroshield and imaged using an Olympus FLV1200 confocal microscope at 10× objective. For each spheroid, 10 μm sections along the z-axis were obtained. Linear attenuation correction and background subtraction of fluorescence intensity were done in FLV1200® software and images were exported for analysis in Image J 1.39. A macro created in Image J was used to locate the center of the spheroid from the DAPI channel and to quantify the fluorescence intensity in the FITC channel. DAPI dye is a small molecule that diffuses rapidly into the spheroid and binds to cell nuclei, hence by using DAPI and FITC the spheroid shape and the distribution of nanoparticle fluorescence are easily determined. If FITC fluorescence is low or inhomogeneous, especially in deep sections of the spheroid then the spheroid shape is not resolved clearly by the thresholding algorithms. In such cases DAPI dye provides the advantage of locating the spheroid. First, the center and periphery of the spheroid was found by thresholding the images from the DAPI channel. This information was used to quantify fluorescent intensity along a straight line (with length equal to the radius of the spheroid) from the images in the FITC channel. The line was rotated by a 10° angle and the procedure was repeated. This procedure was adopted to minimize location-related variability within a spheroid.[42] A total of three spheroids per each case were analyzed and change in intensity profile with spheroid depth was normalized to intensity at the outer perimeter. Once the intensity curves were obtained, the linear trapezoidal rule was used to calculate the area under the curve (AUC). Another parameter, $W_{1/2}$, half width maximum of concentration was calculated based on the distance in the spheroid at which the total concentration (sum of C_b, C_i, and C) was reduced by 50% (depth, x, relative to the spheroid radius, R). A higher AUC value denotes an increase in the number of nanoparticles in a spheroid whereas a smaller $W_{1/2}$ indicates deeper penetration (or steeper concentration decrease). The AUC and $W_{1/2}$ from the images were compared to the predictions from the model. Additionally, a fraction of data points from model predictions were measured to calculate the percentage within 95% CI of experimental data.[43]

5 | MCMC SIMULATIONS

5.1 | Experimental measurements of nanoparticle uptake were imported to MATLAB

Data points between each measured time-period were generated using cubic spline interpolation (MATLAB 13.0®, Math Works, MA). A total of 1000 data points were used in the solution of the inverse problem with the MCMC algorithm. The simulation was run in MATLAB along with the ODE solver for solving the differential equations. For the MCMC simulation, proposal distribution was drawn from a random walk. The default number of states was $N = 1E5$ and the random walk step was $w = 0.01$. In the simulation, the standard deviation was set at 1% of maximum measurement value. The chosen parameter set of uptake rate constants with their respective upper and lower limits used for uniform priors is shown in Table 1. It must be noted that the upper and lower bounds represent a wide range of cell uptake constants. From an initial guess given by the user, Equations (9) and (10) were solved using the ode15s solver in MATLAB. The estimated concentration from initial guess was then compared to the experimental data to evaluate the error and an acceptance factor. Based on the acceptance factor, Markov chain was advanced to choose a new parameter

TABLE 1 Lower and upper bounds chosen for different parameter values

	Lower bound	Upper bound
k_a (M^{-1} min^{-1})	1.00E+00	1.00E+08
k_d (min^{-1})	2.20E−07	2.20E−01
k_e (min^{-1})	2.20E−06	2.88E−01
k_{rec} (min^{-1})	8.00E−06	9.30E−02

Note: The values were chosen from different literature studies and the maximum and minimum values were extended by 10% to form the bounds.[30,52,107]

set. Initial iterations of the Markov chain were discarded (burn in period) and the simulation was run until the Markov chains of all parameters reached equilibrium. The robustness of the Monte Carlo method was assessed by choosing various initial guesses for each parameter and from the potential scale reduction factor (PSRF), which is the ratio of the variance of the posterior estimates and in-chain variance. Ideally, PSRF should be close to 1.

A well-mixed chain is a Markov process near its equilibrium distribution. In the process, the prediction of the next event depends on the previous events. The progression to equilibrium is a sequential dependence on adjacent events that is defined as a "chain." Parameter k_a and k_d estimates showed well-mixed Monte Carlo chains (supplemental data) with small fluctuations around the mean predicted value of the parameters. The Markov Chain for k_i required some burn in, but was well-mixed locally, the predicted values in the burn in period were discarded and only values towards the end were considered. Poor mixing of the chain was observed for the parameter k_{rec}. However, after a long burn in time, that is, 4E4 iterations, all chains appeared to converge towards the mean parameter value. The PSRF for k_a and k_d was 1, for k_i it was 0.87 and 0.61 for k_{rec}. The prediction of parameters was also not dependent on initial guess, all parameters converged to within 10% deviation from the mean parameter value for initial guesses that were an order of magnitude (in some cases 2–3 orders of magnitude) apart (supplemental data). These results indicate the robustness of the MCMC method in fitting the experimental data.

6 | CELL UPTAKE EXPERIMENTS AND MCMC PREDICTIONS

Cell uptake of nanoparticles occurs primarily via energy dependent mechanisms, such as endocytosis (non-specific, specific/receptor mediated), pinocytosis and macropinocytosis. These processes are dependent on binding of nanoparticles to the cell membrane and subsequent internalization through membrane wrapping and "pinch-off" into the cell. The interaction of nanoparticles with a cell is primarily determined by the protein corona that forms on the nanoparticle surface due to the adsorption of proteins that are present in incubation media (cell culture and plasma). From the above described events, it is clear that temperature plays a very important role in (1) the physical processes that affect nanoparticles, such as aggregation, (2) protein adsorption on the nanoparticle surface, and (3) nanoparticle interaction with the cell membrane.[44] The effect of nanoparticle surface functionalization on uptake by Skov-3 cells is shown in Figure 1. The comparison of experimental data and uptake kinetics determined from the parameters predicted by the MCMC simulation are shown. MCMC predictions of cell uptake agree well with experimental results.

Silica nanoparticles modified with mPEGSi and cPEGSi had the same size (~58 nm diameter) and surface potential (~−6 mV @ pH 7.4) (supplemental data). However, mPEGSi particles showed less uptake compared to cPEGSi particles (Figure 1). Carboxy groups have been shown to be more reactive than methoxy groups and hence show more cell uptake than the mPEGSi particles.[45] This is not surprising since in complex media the zeta potential is determined by the formation of a protein corona. Tenzer et al.[46] observed that silica nanoparticles with oppositely charged functional groups (-NH$_2$: positive; -COOH: negative) reached the same zeta potential on incubation with plasma. However, the composition of protein corona was different between two types. This ultimately decides the interaction of nanoparticles with the cells. Likely, the mPEGSi particles interact weakly with the cell surface as seen from the predicted value of dissociation constant k_d, 5.14E2 M and therefore also have a low internalization rate (Table 2). cPEGSi particles show strong binding to the cell surface (k_d, 6.34E5 M) and higher internalization rate compared to mPEGSi. The exposure of cells to hyperthermia at 43°C for 1 h led to faster binding of nanoparticles to cell membrane compared to binding at 37°C for both mPEGSi and cPEGSi. This can be seen from the initial slope (0–1 h) of the uptake kinetics curve at 43°C which is steeper compared to uptake at 37°C (Figure 1). With hyperthermia, the predicted association rates for both PEG types were almost twice the values predicted at 37°C. However, hyperthermia did not increase the number of
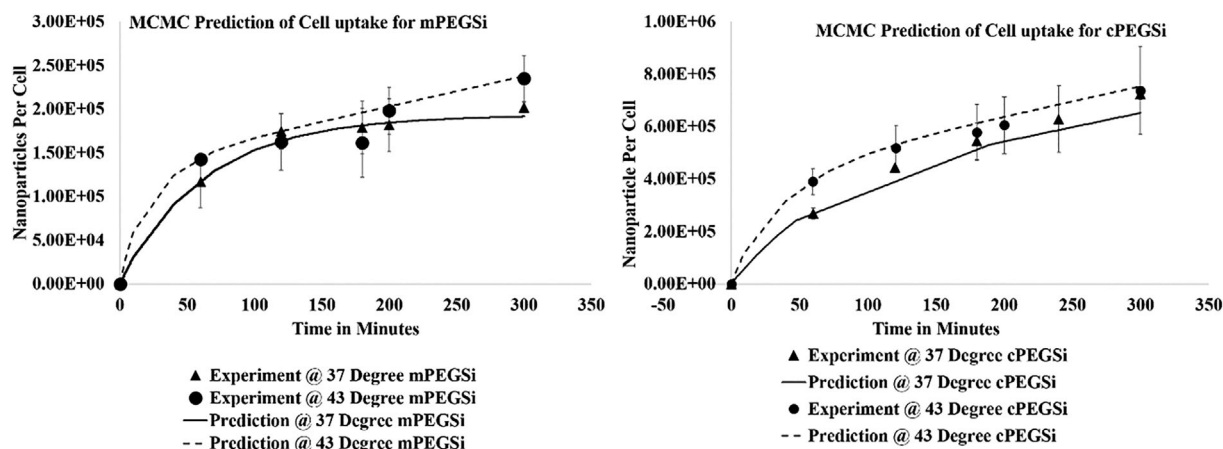
FIGURE 1 Experimental and simulations of mPECSi NP (left) and cPEGSDi NP (right) uptake by cells. MCMC predictions align closely with experimental measurements for all cases. Plots show predictions of cell uptake overlaid with experimental data

TABLE 2 MCMC predictions of different uptake parameters for mPEGSi and cPEGSi in Skov-3 at 37°C and 43°C

	Predicted value	+99% CI	−99% CI	Predicted value	+99% CI	−99% CI
	mPEGSi@37°C			mPEGSi@43°C		
k_a	9.45E+00	9.41E+00	9.49E+00	1.94E+01	1.92E+01	1.97E+01
k_d	1.84E−02	1.83E−02	1.85E−02	5.49E−02	5.40E−02	5.58E−02
k_i	9.10E−05	8.29E−05	9.90E−05	2.52E−03	2.48E−03	2.56E−03
k_{rec}	3.85E−03	3.58E−03	4.12E−03	4.52E−05	3.78E−05	5.26E−05
	cPEGSi@37°C			cPEGSi@43°C		
k_a	7.46E+03	7.30E+03	7.62E+03	1.43E+04	1.41E+04	1.45E+04
k_d	1.18E−02	1.14E−02	1.21E−02	3.03E−02	2.95E−02	3.10E−02
k_i	1.37E−03	1.35E−03	1.39E−03	2.72E−03	2.66E−03	2.78E−03
k_{rec}	1.94E−05	1.81E−05	2.07E−05	2.15E−04	2.02E−04	2.27E−04

Abbreviation: CI, confidence interval.

nanoparticles taken up by cells as no significant difference was found between nanoparticle content at 5 h for 43°C and 37°C. This is because the cells have a finite capacity for nanoparticle internalization and membrane turnover after internalization. The metabolic processes such as lysosome production have been shown to increase with temperature rise from 4°C to 37°C to accommodate more nanoparticles into the cell. However, these processes seem to plateau after 37°C and a further rise in temperature did not cause a significant increase in lysosome production.[47] Our results are consistent with recent observations by DeWitt et al.[48] which showed that the cell uptake of cisplatin was increased in cells at 42°C. No such temperature dependent increase was observed in the uptake of cisplatin conjugated carbon nanotubes. From the experimental measurements and predicted values of internalization (k_i) and externalization rate constants (k_{rec}) it can be observed that for cPEGSi particles, kinetic processes at 43°C are faster than at 37°C. Interestingly, for mPEGSi, hyperthermia caused an increase in k_i whereas k_{rec} decreased.

7 | SIMULATING NANOPARTICLE TRANSPORT IN SPHEROIDS UNDER HYPERTHERMIA

Nanoparticle transport in avascular tumor spheroids depends on particle size, particle uptake by the cells (i.e., k_d) and tumor porosity. The effects of hyperthermia on particle properties and cell uptake have been discussed above. Depending on the thermal dose, hyperthermia related thermal damage causes cell death via apoptosis or necrosis.[20,21] Thermal damage to tumor tissue is modeled by the well-known Arrhenius equation.

$$\Omega(r,T) = F \int_{o}^{t_{\exp}} \exp\left(-E_a / RT_t(x,y,t)\right) dt \tag{16}$$

In Equation (16), F is the frequency or pre-exponential factor (1/s), E_a is the activation energy barrier (J/mole), R is the universal gas constant (J mol^{-1} K^{-1}), and $T_t(x, y, t)$ is the absolute tissue temperature at the specified coordinates. The value of Ω is zero before application of the thermal energy. At $\Omega = 1$, 63% protein denaturation occurs and at $\Omega = 4$, 98% protein denaturation occurs.[49]

Cell death in spheroids from hyperthermia causes an increase in the available fluid fraction (i.e., porosity) for the nanoparticles to access. Therefore, hyperthermia may enhance the transport of nanoparticles into tumor spheroids.[50] Equation (17) describes the change in porosity as a result of cell death under hyperthermia conditions.[49]

$$\varepsilon_{43} = \varepsilon_{37} + (100\% - \varepsilon_{37}) \times (1 - S[r,T]) \tag{17}$$

$S(r, T)$ is cell survival rate which is related to the Arrhenius parameter Ω by

$$S(r,T) = e^{-\Omega/4} \tag{18}$$

Modeling nanoparticle transport as a function of porosity change in response to the application of hyperthermia requires solving a system of coupled nonlinear partial differential equations. The scheme used in modeling the transport of nanoparticles in tumor spheroids was: (i) solve Fick's equation with reaction terms, (ii) model heat generation and thermal damage, (iii) calculate changes in porosity (ε) and the uptake constants, (iv) iterate until the stopping criteria is reached. The system of equations was solved using COMSOL 4.2a. Equations (1), (2), (6), and (7) were solved with corresponding initial and boundary conditions using equations for the transport of diluted species. Equation (16) was solved using the partial differential module with free form scripting (ODE DAE). Free form scripting in COMSOL allows the user to input custom differential equations and their boundary/initial conditions. Since the equations for thermal damage are not available in COMSOL, ODE DAE had to be used to model the thermal damage using the Arrhenius equation. The temperature profile was obtained from the incubator by placing a thermocouple in a well of a 96 well plate containing media. The discrete temperature values at various time points were imported to COMSOL and a continuous profile was generated by interpolation. The tumor spheroid was modeled as a 2D circle with another concentric circle of radius ($R + 100$ μm) as the outer domain of the spheroid. A free triangular mesh was used for both domains (i.e., spheroid and outer domain). The mesh of the outer domain was finely resolved (max element size: 10 μm and min element size: 1.2 μm) in order to account for concentration discontinuity, or "jump" at the boundary. The spheroid domain was meshed with max element size equal to 90 μm. The transport simulations for different cases, that is, cPEGSi at 37°C and 43°C, were simulated for 24 h. The values of different parameters used in the model are presented in Table 3.

8 | SIMULATION AND EXPERIMENTAL RESULTS

A dynamic diffusion model was used to account for particle aggregation under hyperthermia. cPEGSi particles were incubated in DPBS at 43°C and size measurements at various time-points (starting at 1–24 h) were obtained with a Malvern Zetasizer. The size was converted to effective diffusion coefficient using Equation (2). The effective diffusion coefficient increases initially until 6 h due to increase in porosity because of cell death (Figure 2). After 6 h, the diffusion coefficient reduces due to an increase in particle size due to aggregation. Then, a further decrease in cell viability contributes to an increase in the effective diffusion coefficient (Figure 2). The abrupt change in diffusion coefficient is due to shifting equilibrium of colloidal systems in complex media. The repulsive forces between charged nanoparticles keep them in quasi-equilibrium. In the present case, incubation of silica nanoparticles in cell culture medium shifted the equilibrium towards the isoelectric point (0 mV zeta potential) due to adsorption of proteins on the nanoparticle surface. At this point, the quasi-equilibrium is overcome by particle aggregation and a sudden collapse of the colloidal system. This effect is visible in the steep decline of effective diffusion coefficient due to rapid increase in size. Biologically, this trend is not expected in-vivo as particle distribution and stability will be determined by particle cell

TABLE 3   Parameter values used in modeling

Parameter	Value [unit]	Description
R	300E−6 [m]	Spheroid radius
β_{max}	1.3E−7 [mol L^{-1}]	Cell surface binding capacity of spheroids
C_{Medium}	1.13E−9 [mol L^{-1}]	External Boundary Condition
k_B	1.38E−23 [m^2 kg (s^{-2} K^{-1})]	Boltzmann constant
μ	8.94E−4 [Pa s]	Viscosity of fluid (media)
a	30 [nm]	Particle radius
r_p	0.003*R[27]	Collagen fiber radius
λ	a/r_p	Ratio of nanoparticle radius to pore size
Ax	1.19E38 [s^{-1}][50]	Activation energy
EAx	2.57E5 [J mol^{-1}][50]	Activation energy barrier
R	8.31 [J mol^{-1} K^{-1}]	Universal gas constant
ε	0.03	Porosity

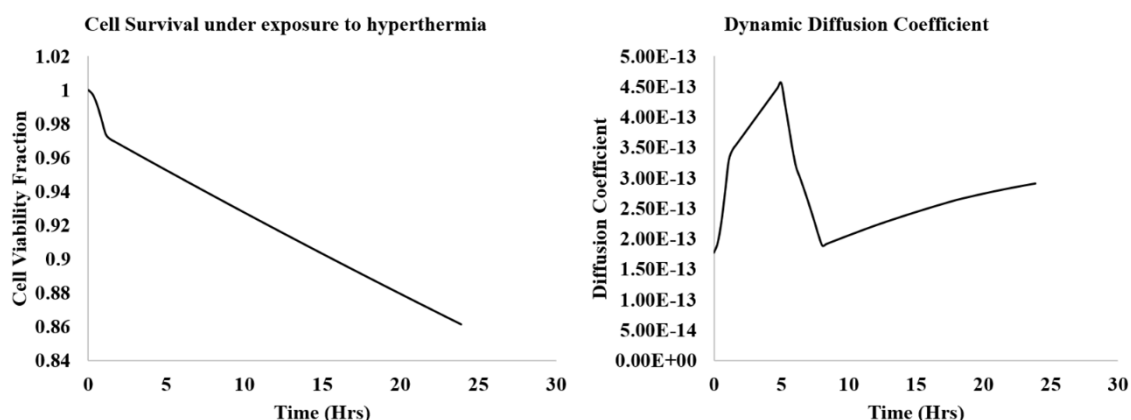Note: Values that could not be measured were adopted from the literature.

FIGURE 2   Plots showing reduction in cell viability under hyperthermia (left) and changes in effective diffusion coefficient as a result of particle aggregation and change in porosity (right)

interactions, protein adsorption and convective forces due to fluid circulation. A continuous examination of particle size variation in complex media instead of discrete size measurements such as those obtained in this study is likely to yield a better representation of particle aggregation kinetics.

Spheroid images showed a sharp drop-off of fluorescence at the periphery. This is due to the loss of nanoparticles (and thus FITC) at the periphery during washing and processing steps. To account for this, a window function was introduced in the model.[51] It can be seen from Figure 3 (top) that after 24 h incubation of cPEGSi at 37°C particles are localized around the periphery of the spheroid. The moving front of fluorescence drops sharply at a 30% distance from the periphery and does not progress further towards the center. These findings indicate that diffusion of cPEGSi in Skov-3 spheroids was a slow process (occurring over hours) and limited to the first few cell layers. Alternatively, spheroids incubated with cPEGSi at 43°C showed a less pronounced front and more diffuse fluorescence after 24 h throughout the spheroid (Figure 3, bottom).

Interestingly, under hyperthermia, MCMC predictions estimated an increase in k_d which should slow the transport of nanoparticle transport. Concurrently, the internalization rate constant increased at 43°C. This leads to depletion of nanoparticles in the interstitial space of the spheroid which maintains the concentration gradient and drives the diffusion of nanoparticles. Furthermore, cell death due to thermal damage increased available fluid fraction for the nanoparticles to diffuse (Table 3, Figure 4). The mean AUC and $W_{1/2}$ values calculated from the experiments agree with the values predicted from simulations (Table 4). The AUC at 43°C was significantly higher than the AUC value at 37°C.
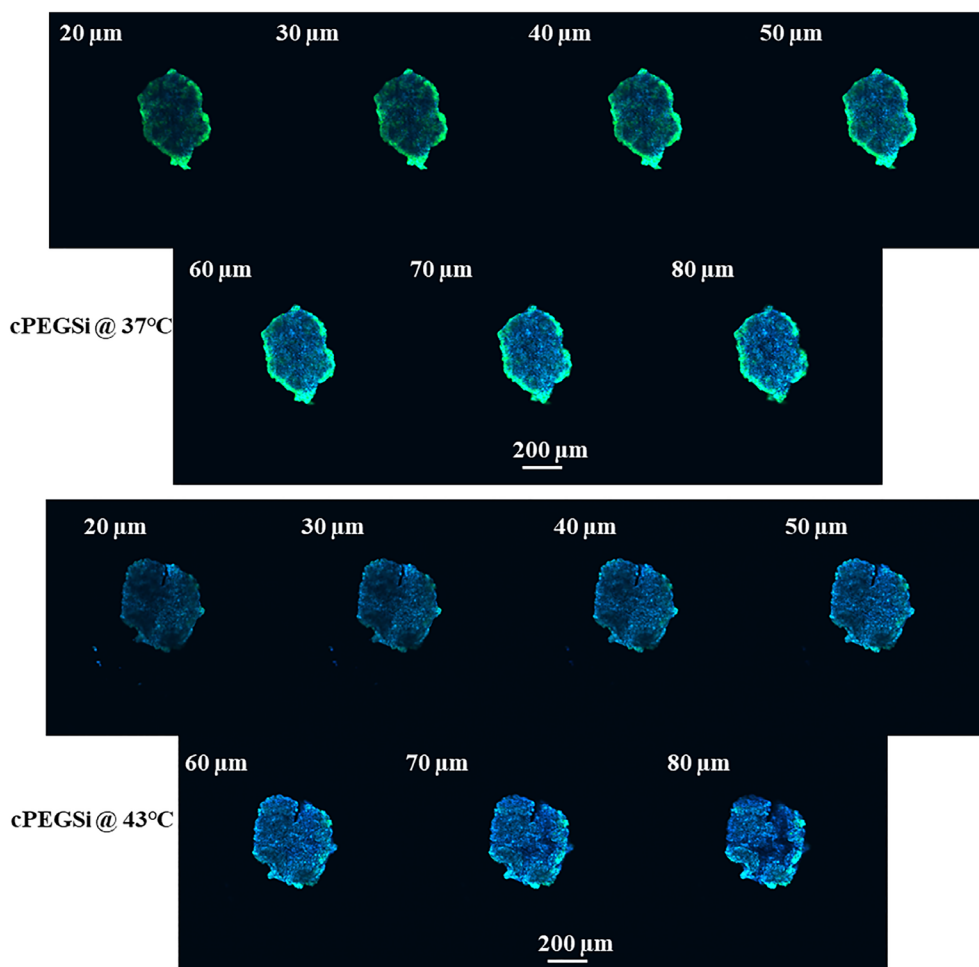
FIGURE 3 Confocal sections of Skov-3 spheroids incubated with cPEGSi at 37°C (top) and 43°C (bottom) with DAPI and FITC channels merged. FITC fluorescence is concentrated around the periphery of the spheroid
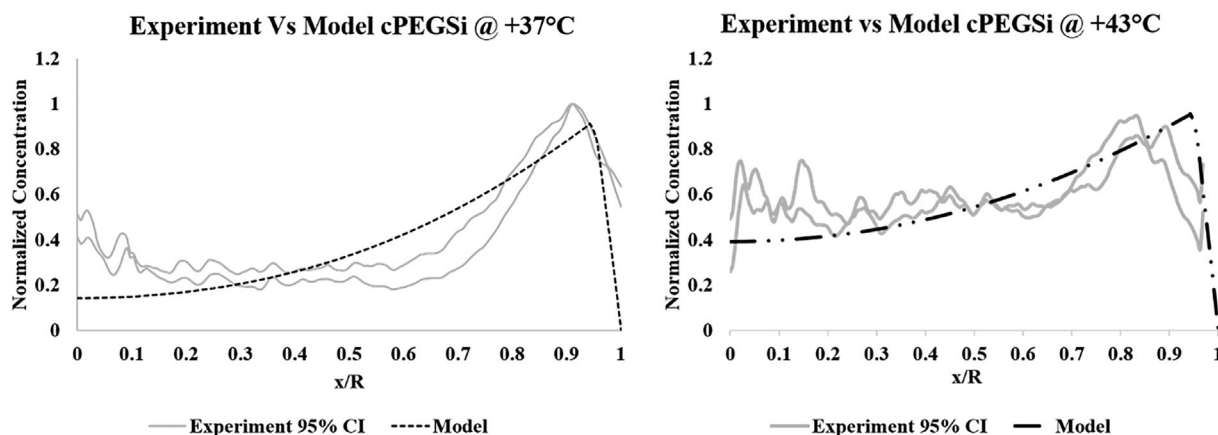

FIGURE 4 Overlay of model predictions with experimental data. The experimental data plotted as two curves denote the higher and lower limits of standard error ($n = 3$)

Nanoparticles also penetrated deeper into the spheroid under hyperthermia (~51% at 43°C from ~32% at 37°C, Table 4). However, no significant difference was found between the $W_{1/2}$ values for the two cases, likely owing to variability of the experimental data. A comparison of simulated and experimental data showed that 55% and 67% values of simulated data points fall within the 95% CI of experimental data at 37°C and 43°C, respectively (Table 4).

TABLE 4 Comparison between experimental determination and model prediction of area under the curve (AUC) and $W_{1/2}$ (x/R) values from cPEGSi transport in Skov-3 spheroids

	AUC	$W_{1/2}$	Fraction 95% CI
Experiment@37°C	0.34 ± 0.06	0.68 ± 0.15	$55 \pm 8\%$
Simulation@37°C	0.38	0.66	
Experiment@43°C	0.61 ± 0.11	0.49 ± 0.12	$67 \pm 5\%$
Simulation@43°C	0.57	0.43	

Note: R is the spheroid radius and *x* is the depth from the spheroid periphery. The fraction indicates percentage of model simulated data points that are within the 95% confidence limits of experimental data.
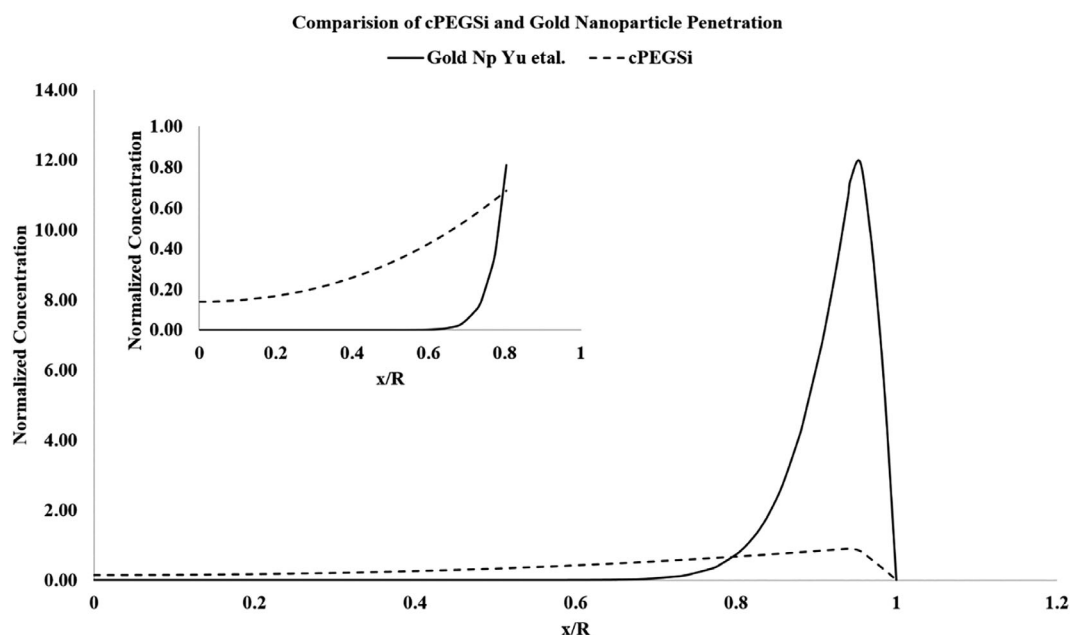

FIGURE 5 COMSOL simulations comparing transport of 50 nm gold nanoparticles with high cell binding affinity to cPEGSi with lower cell binding affinity. The uptake parameters for gold nanoparticles were from Jin et al.[52] The inset shows the particle distribution (zoomed) inside the spheroid

The results show that diffusion is the rate limiting step for cPEGSi transport instead of the reaction parameters of cell uptake. The moving front progresses into the spheroid as long as free nanoparticles are available at the tumor surface. If the nanoparticle concentration drops to zero at the periphery, that is, when nanoparticles are removed via washing the spheroids or in vivo when nanoparticles are removed at the tumor site due to plasma clearance, the front appears to be stuck at some distance from the periphery. In the case of high binding affinity, transport is rate limited by the reaction rate of nanoparticle association. A comparison to gold nanoparticle transport (~50 nm in diameter) with uptake rate constants obtained from the literature,[52] shows that high association, that is, k_a of 7.2E7 M^{-1} s^{-1}, leads to high accumulation at the periphery and low penetration into the tumor (Figure 5). High accumulation at the periphery results in the "binding site barrier" effect which further impedes diffusion into the spheroid.[25] On the other hand, low affinity leads to deeper penetration of nanoparticles.

9 | DISCUSSION

Computational approaches have contributed to a better understanding and improved designs of nanoparticle drug delivery systems. Mathematical models of nanoparticle transport at the tumor level (spheroids, 3D models) have been developed[29,53–57] and there are several fine reviews.[58–61] The approaches span from modeling nanoparticle cell interactions,[62–64] models that mimic the vasculature and tumor microenvironment,[65] pharmacokinetics models,[66–69]

pharmacokinetics models that include vascular flow[70,71] and up to multi-scale models that combine whole body pharmacokinetics with nanoparticle-tumor cell interactions.[72,73] According to current literature, only one other author has reported the mathematical prediction of temperature dependent cell uptake of nanoparticles. The model formulated by Zhang et al.[74] studied the temperature dependent (6°C–40°C) uptake of quantum dots in SPCA-1 cells (lung adenocarcinoma) and showed the presence of a temperature independent component of internalization at low temperatures. Based on the rate constants obtained by fitting Langmuir kinetics to experimental data, they show that with an increase in temperature from 22°C to 37°C, there is a reduction in k_a, an increase in k_d and a plateau in k_i. However, the experimental data by the authors showed a marked increase in uptake at 37°C. This is counterintuitive as the total content of nanoparticles measured in a cell can only increase when there is an increased association of particles with the cell membrane or if there is increased internalization of particles by the cells. The variability in the kinetics of temperature dependent cell uptake of nanoparticles as studied by different authors[47,48,74] suggests that this phenomenon may be dependent on the type of nanoparticle and the cell line. The MCMC method used here for predicting cell uptake rate constants provides a unified/general framework for parameter estimation without the need for additional experiments or the need to make specific *a priori* assumptions regarding cell uptake phenomenon. Since this approach can predict all rate constants with good confidence and is robust (supplemental data), extending it to other nanoparticle systems (liposomes, gold nanoparticles, etc.), various cell lines and different conditions can be done easily.

The finite element method (FEM) developed in this work is an improvement over existing models of nanoparticle transport. FEM's advantages are that it can easily deal with irregular 3D geometries and is more accurate than finite volume methods because of lower numerical dissipation. It can easily use higher order basis functions (p-refinement), and thus, is superior when dealing with a diffusion term that can have high gradients, and its convergence is mathematically assured. FEM models for nanoparticle transport in tumor spheroids have been described in the literature for, (1) effect of collagenase on spheroid disruption and subsequent effect on nanoparticle transport,[51] (2) dynamic diffusion model of liposomal transport in spheroids,[54] and (3) macroscopic transport model of heat conduction and magnetic nanoparticle transport in spheroids.[50] The first two models used the conventional method to calculate cell uptake parameters, that is, perform cell experiments at 4°C to estimate k_a and k_d and use the information at 37°C to estimate k_i. However, the models only consider nanoparticle transport through the tumor and does not consider uptake by the cells.

Modeling uptake of nanoparticles by the cells in a spheroid is critical to designing therapeutic interventions for cancer as the drug has to reach the intended target inside the cell to cause an effect. Additionally, the effect of heat on nanoparticle stability and uptake has not been considered until now. By combining MCMC predictions and finite element simulations, several scenarios can be simulated to find an optimal balance between penetration and cell uptake (MCMC predictions). The transport of drugs to tumors happens through convection which is followed by extravasation of the drug at the tumor site. As mentioned previously, the transport after extravasation is determined by the diffusion into the tumor and the uptake rate of the cells. The uptake rate of nanoparticles is in-turn dependent on the surface and physical properties of the nanoparticle. The combination of parameter estimation using inverse techniques and finite element methods is a suitable approach for this multiphysics problem. Based on the model predictions, the density/type of surface coating (i.e., number of moieties) and drug loading in nanoparticles can be determined to achieve an efficient therapeutic response. For example, as seen in our experiments, the type of surface coating (i.e., mPEG vs. cPEG) plays an important role in determining the uptake. In our case, mPEG particles are not a suitable choice for surface modification due to low cell uptake (Figure 1) since they appear to interact weakly with the cell surface. PEG moieties generally possess a stealth advantage since they can avoid being tagged by proteins (opsonization), and, thus, being recognized by the reticuloendothelial system (RES) and cleared by the immune cells. However, the same property proves as a detriment to cell uptake. Tagging of nanoparticle surface with proteins promotes cellular recognition, attachment, and uptake. Hence, the reactive end groups of PEG are important. Methyl group, which is inert, is not reactive hence induces less cell uptake. Carboxy group is more reactive and therefore exhibits more cell uptake.

The observations from experiments and the corresponding models present important factors that need to be considered for nanoparticle transport in solid tumors under hyperthermia. These include the effect of hyperthermia on stability of nanoparticle formulation, uptake of nanoparticles by the cell exposed to hyperthermia and the effect of tumor microenvironment on nanoparticle penetration. Colloidal stability, that is, aggregation, is a kinetic phenomenon dependent on temperature (Figure 2). Poor colloidal stability on exposure to hyperthermia may compromise the therapeutic efficacy by further impeding nanoparticle penetration. From a cell uptake perspective, if hyperthermia increases the association rate of particles with the cell, it may overcome the diffusive transport and impede the transport of nanoparticles into the spheroid. Experiments in spheroids demonstrated that in the absence of hyperthermia, particles

mainly localized around the tumor periphery, whereas exposure to hyperthermia lead to penetration of nanoparticles into the spheroid (Figure 3), likely due to an increase in ECM porosity or decreased ECM viscosity at higher temperatures. The AR model showed that the transport of pegylated silica nanoparticles is diffusion dominated (Figure 4). The predictions of the model and experiments agreed with each-other (Table 4). Since spheroids and cells can be cultured in a high throughput format, the combination of a mathematical model with high throughput experiments will allow for rapid screening of nanoparticle systems for therapeutic applications.

10 | MODEL LIMITATIONS AND OPPORTUNITIES FOR IMPROVEMENT

The experimental data points vary from model predictions at the center of a spheroid for both 37°C and 43°C cases and fluorescence intensity from silica nanoparticles increased near the core of the spheroid (Figure 5). This may be due to increased porosity owing to cell necrosis at the center of the spheroid. A similar profile of increased fluorescent intensity at the middle of a spheroid due to increased porosity as a result of cell necrosis in the region was reported for Hela cell spheroids (400 μm diameter).[51] In the current study, we were not able to accurately estimate the amount of silica nanoparticles which are lost from spheroid periphery during experimental manipulation (washing) and imaging. The local structural variations in porosity are also not known and hence porosity was assumed to be homogeneously distributed. The estimation of radially dependent porosity is difficult since reliable techniques for porosity estimation are not available. Electron microscopy (SEM and TEM) has been used to image the microstructure of a spheroid and estimate porosity. However, the processing of spheroids for SEM and TEM, mainly dehydration and critical drying, leads to shrinkage of tissues and alteration to spheroid structure. Furthermore, the alteration in cell uptake of nanoparticles due to aggregation under hyperthermia cannot be estimated inside the spheroid. In monolayer cultures, the uptake was saturated at 5 h and therefore aggregation which happens after 6 h did not affect cell uptake. In spheroids, the cell uptake within deep cell layers is delayed due to diffusion. Future models may consider the aforementioned factors for increasing the agreement between experimental data and model predictions.

The spheroid model used does not present the true complex tumor micro-environment and ECM. The extent and complexity of the tumor microenvironment and function of the ECM has been reviewed elsewhere.[75,76] Particles experience opsonization and uptake by macrophages in the plasma leading to extravasation by the liver and spleen. Biological barriers to transport exist throughout the body that inhibits nanoparticle transport from the vasculature to tumor tissue, including the capillary endothelial layer, tissue microenvironment, and finally the membranes of the target cells and organelles.[77–79] Based on a purely computation approach, Hauert et al.[80] propose that nanoparticle design should include a mechanism that delays nanoparticle binding until after they have had time to diffuse deep into the tumor. Others have proposed multi-stage nanoparticles to improve the potential for the nanoparticles to reach and to transport deep into the tumor.[81] Based on a purely mathematical models, Stylianopoulos et al.[82] propose that cationic nanoparticles should have better transport into tumors. Dai et al.[83] conducted a very comprehensive study and found that, on average, only 0.59% and 0.25% of targeted and non-targeted nanoparticles, respectively, injected into tumor-bearing mice reached the tumor, and as little as 0.001% (of active) and 0.003% (passive) nanoparticles actually reached the cancer cells. Even more interesting, of the nanoparticles that enter the tumor, only about 1% were associated with cancer cells, about 9% were with tumor associated macrophages and the rest remained extracellular. The finding was consistent for both gold and silica nanoparticles, targeted and non-targeted and for different size nanoparticles. In the present study the spheroids only included cancer cells. However, Priwitaningrum et al.[84] developed a "heterospheroid" model to evaluate nanoparticle transport in spheroids containing both cancer cells and fibroblasts and obtained data that support the findings of Dai et al.[83] Nevertheless, more advanced three-dimensional tumor models with multiple cell types, more complete ECM and microvasculature better resembling the in vivo tumor microenvironment are needed.

Another aspect of tumor spheroids that differs from solid tumors in vivo is the total lack of a vasculature. In vitro avascular tumor spheroids possess pH and pO_2 gradients which are dependent on cancer cell type,[13] but which is not as steep as in in vivo solid tumors. Helmlinger et al.[14] found that mean interstitial pH and pO_2 in solid tumors reduced from ~7.3 and 14 mmHg respectively at the interface between the nearest blood vessel and the tumor, to ~6.7 and 0 mmHg respectively at the core. The "reversed pH gradient", in which extracellular pH is more acidic than intracellular pH has been considered as a mechanism to trigger drug release in solid tumors. Al-Husari et al.[15] modeled intracellular pH regulation and pO_2 and pH gradients in early tumor growth which accounts for a necrotic core, quiescent layer and proliferating outer core. The model predicts the effect of oxygen, pH and lactate on tumor growth and

nutrient consumption on tumor morphology. The spheroids in the present study did exhibit a necrotic core but neither the pH nor pO_2 were measured. However, it is highly likely that the spheroids exhibited expected pH and O_2 gradients. Tumor-on-chip models are commercially available that add a vascular element, which should be considered for future experiments.

The details of the interaction of nanoparticles containing a PEG surface with proteins and macrophages have been extensively investigated.[85] A method for the precise quantification of nanoparticle internalization to cancer cells has contributed to the understanding of the factors that affect nanoparticle drug delivery systems.[31] The internalization of liposomes is dependent on both size and charge.[86] Attaching polyethyleneglycol (PEG) to a nanoparticle's surface has been the most widely used approach to avoid opsonization and prolong nanoparticle plasma residence time.[87–91] However, PEG has been shown to interfere with a nanoparticle traversing the ECM and suppress interaction with the cell membrane for effective cellular uptake.[31,75,92–95] Labouta et al.[96] characterized these interactions recognizing that PEG confirmation affects the interactions of liposomes with the ECM and therefore their transport behavior. Strategies have been proposed to evade the RES and the so-called "PEG dilemma" either by modifying the nanoparticle surface or the ECM.[97,98] The present study demonstrated that methoxy-PEG-silane (mPEGSi) are taken up less efficiently than carboxy-PEG-silane (cPEGSi) particles. Gyenge et al.[99] found that SiO_2-PEG nanoparticle uptake to cells was minimal after 24 h compared to SiO_2-OH and SiO_2-NH$_2$ nanoparticles. Bachir et al.[100] showed that accumulation of nanoparticles in macrophage cells decreased with increasing the mPEG surface density or the mPEG molecular weight suggesting that mPEG may be a better choice to avoid the RES, but that cPEG may be a better choice to enhance cancer cell uptake. Nevertheless, additional experiments with different types of particles and different surface coatings are warranted.

The present study only evaluated one nanoparticle size. Gaumet et al.[101] provided a review of reports of fenestration sizes in different organs indicating 200–780 nm in mouse tumors compared to <6 nm in skeletal, cardiac and smooth muscle, 150 nm in liver and spleen and 1–400 nm in lungs. Sindhwani et al.[102] provided evidence that the gaps between capillary endothelial cells account for only 3% of nanoparticles entering tumors, the rest crossing the capillary wall by active processes of transcytosis. This finding is bound to be controversial as it is inconsistent with numerous studies that claim that the gaps are indeed responsible for the enhanced uptake of nanoparticles in many tumors. Nevertheless, it does complicate the assumptions made with respect to the optimal nanoparticle size for solid tumor therapy and thus further investigation is warranted. For example, detailed analysis of nanoparticle transport through solid tumors in vivo with particular attention to the orientation and characteristics of the tumor-associated vasculature will shed light on this problem. Recent efforts by Cattaneo and Zunino[103] and Shipley et al.[104] aimed to solve this issue through multiscale modeling of fluid and drug distribution in vascular tumors.

Finally, this study simulated a "slow-rate," "mild" application of hyperthermia administered on the order of an hour. However, hyperthermia therapy for cancer can also be administered faster with greater localization by adding a thermal component to the nanocarrier and stimulating with an external source (such as near-infrared light[20,21] or alternating magnetic field[105]). A recent study by Wang et al.[106] used Monte Carlo simulations to study local heat generation from graphene nanosheets and the corresponding photothermal damage to cells. Such approaches can be used to model the effects of a localized "fast-rate" application of hyperthermia in tumor spheroids.

11 | CONCLUSIONS

Drug delivery to avascular tumors is a challenging problem that has been addressed by employing carriers, such as nanoparticles and drug–polymer complexes. Computational modeling has improved the understanding of factors that contribute to the transport and delivery of drugs to tumors and ultimate efficacy of the therapy. This study confirms that 58 nm silica (cPEGSi) nanoparticles largely concentrate at the periphery of avascular Skov-3 tumor spheroids, consistent with several other studies, but further demonstrates that tumor penetration can be enhanced with mild hyperthermia (43°C). Cell death due to thermal damage increases available fluid fraction for the nanoparticles to diffuse deeper into the tumor. The mean area under the concentration versus depth curve (AUC) at 43°C was significantly higher than the AUC value at 37°C. The half width maximum of concentration ($W_{1/2}$) increased from ~31% at 37°C to ~50% at 43°C, but the difference was not significant likely because of variability of the experimental data. The finite element simulations compared well to experimental data with 55% and 67% values of simulated data points falling within the 95% CI of experimental data at 37°C and 43°C, respectively. Our results indicate that for cancer cells and spheroids with similar uptake and structural characteristics of Skov-3 Ovarian carcinoma cells, mild hyperthermia has the

potential to overcome the binding site barrier effect. This could improve nanoparticle distribution in Ovarian carcinoma spheroids. Further research into different kinds of ovarian cancer cells and robust combination of experimental platforms and mathematical simulations is needed for developing personalized nanodrugs based on cancer type.

CONFLICT OF INTEREST
All authors declare no conflict of interests.

ORCID
Helcio R. B. Orlande https://orcid.org/0000-0002-3511-322X
Marcelo J. Colaco https://orcid.org/0000-0002-8020-6222
Anthony J. McGoron https://orcid.org/0000-0003-3714-4676

REFERENCES
1. Agarwal R, Jurney P, Raythatha M, et al. Effect of shape, size, and aspect ratio on nanoparticle penetration and distribution inside solid tissues using 3D spheroid models. *Adv Healthc Mater*. 2015;4:2269-2280.
2. Wang H, Zuo Z, Du J, et al. Surface charge critically affects tumor penetration and therapeutic efficacy of cancer nanomedicines. *Nano Today*. 2016;11:133-144.
3. Huang K, Boerhan R, Liu C, Jiang G. Nanoparticles penetrate into the multicellular spheroid-on-chip: effect of surface charge, protein corona, and exterior flow. *Mol Pharm*. 2017;14:4618-4627.
4. Minchinton AI, Tannock IF. Drug penetration in solid tumours. *Nat Rev Cancer*. 2006;6:583-592.
5. Jain RK, Stylianopoulos T. Delivering nanomedicine to solid tumors. *Nat Rev Clin Oncol*. 2010;7:653-664.
6. Dreher MR, Liu WG, Michelich CR, Dewhirst MW, Yuan F, Chilkoti A. Tumor vascular permeability, accumulation, and penetration of macromolecular drug carriers. *J Natl Cancer Inst*. 2006;98:335-344.
7. Yuhas JM, Tarleton AE, Molzen KB. Multicellular tumor spheroid formation by breast-cancer cells isolated from different sites. *Cancer Res*. 1978;38:2486-2491.
8. Rolver MG, Elingaard-Larsen LO, Pedersen SF. Assessing cell viability and death in 3D spheroid cultures of cancer cells. *J Vis Exp*. 2019;16:e59714.
9. Sun M, Lee J, Chen Y, Hoshino K. Studies of nanoparticle delivery with in vitro bio-engineered microtissues. *Bioact Mater*. 2020;5:924-937.
10. Foglietta F, Canaparo R, Muccioli G, Terreno E, Serpe L. Methodological aspects and pharmacological applications of three-dimensional cancer cell cultures and organoids. *Life Sci*. 2020;254:117784.
11. Acker H, Carlsson J, Muellerkklieser W, Sutherland RM. Comparative pO_2 measurements in cell spheroids cultured with different techniques. *Br J Cancer*. 1987;56:325-327.
12. Sutherland RM. Cell and environment interactions in tumor microregions—The multicell spheroid model. *Science*. 1988;240:177-184.
13. Gorlach A, Acker H. pO_2-gradients and pH-gradients in multicellular spheroids and their relationship to cellular-metabolism and radiation sensitivity of malignant human tumor-cells. *BBA Mol Basis Dis*. 1994;1227:105-112.
14. Helmlinger G, Yuan F, Dellian M, Jain RK. Interstitial pH and pO_2 gradients in solid tumors in vivo: high-resolution measurements reveal a lack of correlation. *Nat Med*. 1997;3:177-182.
15. Al-Husari M, Murdoch C, Webb SD. A cellular automaton model examining the effects of oxygen, hydrogen ions and lactate on early tumour growth. *J Math Biol*. 2014;69:839-873.
16. Cottin S, Ghani K, de Campos-Lima PO, Caruso M. Gemcitabine intercellular diffusion mediated by gap junctions: new implications for cancer therapy. *Mol Cancer*. 2010;9:141.
17. Fotopoulou C, Cho CH, Kraetschell R, et al. Regional abdominal hyperthermia combined with systemic chemotherapy for the treatment of patients with ovarian cancer relapse: results of a pilot study. *Int J Hyperthermia*. 2010;26:118-126.
18. van der Zee J. Heating the patient: a promising approach? *Ann Oncol*. 2002;13:1173-1184.
19. Kouloulias VE, Koukourakis GV, Petridis AK, Kouvaris I, Gouliamos AD. The efficacy of Caelyx and hyperthermia for anticancer treatment. *Recent Pat Anticancer Drug Discov*. 2007;2:246-250.
20. Tang Y, McGoron AJ. Combined effects of laser-ICG photothermotherapy and doxorubicin chemotherapy on ovarian cancer cells. *J Photochem Photobiol B: Biology*. 2009;97:138-144.
21. Tang Y, McGoron AJ. Increasing the rate of heating: a potential therapeutic approach for achieving synergistic tumour killing in combined hyperthermia and chemotherapy. *Int J Hyperthermia*. 2013;29:145-155.
22. Nagesetti A, McGoron AJ. Multifunctional organically modified silica nanoparticles for chemotherapy, adjuvant hyperthermia and near infrared imaging. *Colloids Surf B Biointerfaces*. 2016;147:492-500.

23. Nagesetti A, Srinivasan S, McGoron AJ. Polyethylene glycol modified ORMOSIL theranostic nanoparticles for triggered doxorubicin release and deep drug delivery into ovarian cancer spheroids. *J Photochem Photobiol B: Biology*. 2017;174:209-216.

24. Weinstein JN, Eger RR, Covell DG, et al. The pharmacology of monoclonal antibodies. *Ann N Y Acad Sci*. 1987;507:199-210.

25. Graff CP, Wittrup KD. Theoretical analysis of antibody targeting of tumor spheroids: importance of dosage for penetration, and affinity for retention. *Cancer Res*. 2003;63:1288-1296.

26. Thurber GM, Wittrup KD. Quantitative spatiotemporal analysis of antibody fragment diffusion and endocytic consumption in tumor spheroids. *Cancer Res*. 2008;68:3334-3341.

27. Fournier RL. *Basic Transport Phenomena in Biomedical Engineering*. Boca Raton, FL: CRC Press, Taylor & Francis Group; 2018.

28. Truskey GA, Yuan F, Katz DF. *Transport Phenomena in Biological Systems*. Upper Saddle River, NJ: Pearson Prentice Hall; 2009:860.

29. Goodman TT, Chen J, Matveev K, Pun SH. Spatio-temporal modeling of nanoparticle delivery to multicellular tumor spheroids. *Biotechnol Bioeng*. 2008;101:388-399.

30. Wilhelm C, Billotey C, Roger J, Pons JN, Bacri JC, Gazeau F. Intracellular uptake of anionic superparamagnetic nanoparticles as a function of their surface coating. *Biomaterials*. 2003;24:1001-1011.

31. Gottstein C, Wu G, Wong BJ, Zasadzinski JA. Precise quantification of nanoparticle internalization. *ACS Nano*. 2013;7:4933-4945.

32. Orlande HRB. *Thermal Measurements and Inverse Techniques*. Boca Raton, FL: CRC Press; 2011:756.

33. Orlande H, Colaco M, Dulikravich G, et al. State estimation problems in heat transfer. *Int J Uncertain Quantif*. 2012;2:239-258.

34. Orlande HRB, Dulikravich GS, Neumayer M, Watzenig D, Colaco MJ. Accelerated Bayesian inference for the estimation of spatially varying heat flux in a heat conduction problem. *Numer Heat Transf A: Applications*. 2014;65:1-25.

35. Calvetti D, Somersalo E. *Introduction to Bayesian Scientific Computing: Ten Lectures on Subjective Computing*. New York: Springer; 2007.

36. Kaipio J, Somersalo E. *Statistical and Computational Inverse Problems*. New York: Springer; 2005.

37. Gilks WR. Markov chain Monte Carlo. In: Armitage P, Colton T, eds. *Encyclopedia of Biostatistics*. Vol 2. 2nd ed. John Wiley & Sons; 2005. https://onlinelibrary.wiley.com/doi/book/10.1002/0470011815.

38. Zhao X, Bagwe R, Tan W. Development of organic-dye-doped silica nanoparticles in a reverse microemulsion. *Adv Mater*. 2004;16:173-176.

39. Bagwe RP, Yang CY, Hilliard LR, Tan WH. Optimization of dye-doped silica nanoparticles prepared using a reverse microemulsion method. *Langmuir*. 2004;20:8336-8342.

40. Carlsson J, Acker H. Relations between pH, oxygen partial-pressure and growth in cultured-cell spheroids. *Int J Cancer*. 1988;42:715-720.

41. Yuhas JM, Li AP, Martinez AO, Ladman AJ. A simplified method for production and growth of multicellular tumor spheroids. *Cancer Res*. 1977;37:3639-3643.

42. le Roux L, Volgin A, Maxwell D, Ishihara K, Gelovani J, Schellingerhout D. Optimizing imaging of three-dimensional multicellular tumor spheroids with fluorescent reporter proteins using confocal microscopy. *Mol Imaging*. 2008;7:214-221.

43. Wientjes MG, Yeung BZ, Lu Z, Wientjes MG, Au JLS. Predicting diffusive transport of cationic liposomes in 3-dimensional tumor spheroids. *J Control Release*. 2014;192:10-18.

44. Mahmoudi M, Shokrgozar MA, Behzadi S. Slight temperature changes affect protein affinity and cellular uptake/toxicity of nanoparticles. *Nanoscale*. 2013;5:3240-3244.

45. Zhang LW, Monteiro-Riviere NA. Mechanisms of quantum dot nanoparticle cellular uptake. *Toxicol Sci*. 2009;110:138-155.

46. Tenzer S, Docter D, Kuharev J, et al. Rapid formation of plasma protein corona critically affects nanoparticle pathophysiology. *Nat Nanotechnol*. 2013;8:772-781.

47. Mahmoudi M, Abdelmonem AM, Behzadi S, et al. Temperature: the "ignored" factor at the nanobio interface. *ACS Nano*. 2013;7:6555-6562.

48. DeWitt MR, Pekkanen AM, Robertson J, Rylander CG, Rylander MN. Influence of hyperthermia on efficacy and uptake of carbon nanohorn-cisplatin conjugates. *J Biomech Eng Trans ASME*. 2014;136:021003.

49. Chang IA, Nguyen UD. Thermal modeling of lesion growth with radiofrequency ablation devices. *Biomed Eng Online*. 2004;3:27.

50. Attaluri A, Ma R, Qiu Y, Li W, Zhu L. Nanoparticle distribution and temperature elevations in prostatic tumours in mice during magnetic nanoparticle hyperthermia. *Int J Hyperthermia*. 2011;27:491-502.

51. Goodman TT, Olive PL, Pun SH. Increased nanoparticle penetration in collagenase-treated multicellular spheroids. *Int J Nanomed*. 2007;2:265-274.

52. Jin H, Heller DA, Sharma R, Strano MS. Size-dependent cellular uptake and expulsion of single-walled carbon nanotubes: single particle tracking and a generic uptake model for nanoparticles. *ACS Nano*. 2009;3:149-158.

53. Curtis LT, England CG, Wu M, Lowengrub J, Frieboes HB. An interdisciplinary computational/experimental approach to evaluate drug-loaded gold nanoparticle tumor cytotoxicity. *Nanomedicine*. 2016;11:197-216.

54. Gao Y, Li M, Chen B, et al. Predictive models of diffusive nanoparticle transport in 3-dimensional tumor cell spheroids. *AAPS J*. 2013;15:816-831.

55. Liu J, Yan F, Chen H, et al. A novel individual-cell-based mathematical model based on multicellular tumour spheroids for evaluating doxorubicin-related delivery in avascular regions. *Br J Pharmacol*. 2017;174:2862-2879.

56. Swietach P, Hulikova A, Patiar S, Vaughan-Jones RD, Harris AL. Importance of intracellular pH in determining the uptake and efficacy of the weakly basic chemotherapeutic drug, doxorubicin. *PLoS One*. 2012;7:e35949.

57. Miller HA, Frieboes HB. Evaluation of drug-loaded gold nanoparticle cytotoxicity as a function of tumor vasculature-induced tissue heterogeneity. *Ann Biomed Eng*. 2019;47:257-271.

58. Mascheroni P, Schrefler BA. In silico models for nanomedicine: recent developments. *Curr Med Chem*. 2018;25:4192-4207.

59. Shamsi M, Mohammadi A, Manshadi MKD, Sanati-Nezhad A. Mathematical and computational modeling of nano-engineered drug delivery systems. *J Control Release*. 2019;307:150-165.

60. Zhan W, Alamer M, Xu XY. Computational modelling of drug delivery to solid tumour: understanding the interplay between chemotherapeutics and biological system for optimised delivery systems. *Adv Drug Deliv Rev*. 2018;132:81-103.

61. Stillman NR, Kovacevic M, Balaz I, Hauert S. In silico modelling of cancer nanomedicine, across scales and transport barriers. *npj Comput Mater*. 2020;6:92.

62. Slabu I, Roeth AA, Engelmann UM, et al. Modeling of magnetoliposome uptake in human pancreatic tumor cells in vitro. *Nanotechnology*. 2019;30:184004.

63. Shadmani P, Mehrafrooz B, Montazeri A, Naghdabadi R. Protein corona impact on nanoparticle-cell interactions: toward an energy-based model of endocytosis. *J Phys Condens Matter*. 2020;32:115101.

64. Hu J, Youssefian S, Obayemi J, Malatesta K, Rahbar N, Soboyejo W. Investigation of adhesive interactions in the specific targeting of triptorelin-conjugated PEG-coated magnetite nanoparticles to breast cancer cells. *Acta Biomater*. 2018;71:363-378.

65. He H, Liu C, Liu Y, et al. Mathematical modeling of the heterogeneous distributions of nanomedicines in solid tumors. *Eur J Pharm Biopharm*. 2019;142:153-164.

66. Cheng Y, He C, Riviere JE, Monteiro-Riviere NA, Lin Z. Meta-analysis of nanoparticle delivery to tumors using a physiologically based pharmacokinetic modeling and simulation approach. *ACS Nano*. 2020;14:3075-3095.

67. Dawidczyk CM, Russell LM, Hultz M, Searson PC. Tumor accumulation of liposomal doxorubicin in three murine models: optimizing delivery efficiency. *Nanomedicine: Nanotechnol Biol Med*. 2017;13:1637-1644.

68. Miller HA, Frieboes HB. Pharmacokinetic/pharmacodynamics modeling of drug-loaded PLGA nanoparticles targeting heterogeneously vascularized tumor tissue. *Pharm Res*. 2019;36:185.

69. Dogra P, Adolphi NL, Wang Z, et al. Establishing the effects of mesoporous silica nanoparticle properties on in vivo disposition using imaging-based pharmacokinetics. *Nat Commun*. 2018;9:4551.

70. Kirtane AR, Siegel RA, Panyam J. A pharmacokinetic model for quantifying the effect of vascular permeability on the choice of drug carrier: a framework for personalized nanomedicine. *J Pharm Sci*. 2015;104:1174-1186.

71. Lee TR, Greene MS, Jiang Z, et al. Quantifying uncertainties in the microvascular transport of nanoparticles. *Biomech Model Mechanobiol*. 2014;13:515-526.

72. Hendriks BS, Reynolds JG, Klinz SG, et al. Multiscale kinetic modeling of liposomal doxorubicin delivery quantifies the role of tumor and drug-specific parameters in local delivery to tumors. *CPT Pharmacomet Syst Pharmacol*. 2012;1:15.

73. Kashkooli FM, Soltani M, Rezaeian M, Taatizadeh E, Hamedi M. Image-based spatio-temporal model of drug delivery in a heterogeneous vasculature of a solid tumor—Computational approach. *Microvasc Res*. 2019;123:111-124.

74. Zhang A, Guan Y, Xu LX. Theoretical study on temperature dependence of cellular uptake of QDs nanoparticles. *J Biomech Eng Trans ASME*. 2011;133:124502.

75. Peng J, Yang Q, Shi K, Xiao Y, Wei X, Qian Z. Intratumoral fate of functional nanoparticles in response to microenvironment factor: implications on cancer diagnosis and therapy. *Adv Drug Deliv Rev*. 2019;143:37-67.

76. Huai Y, Hossen MN, Wilhelm S, Bhattacharya R, Mukherjee P. Nanoparticle interactions with the tumor microenvironment. *Bioconjug Chem*. 2019;30:2247-2263.

77. Rabanel JM, Aoun V, Elkin I, Mokhtar M, Hildgen P. Drug-loaded nanocarriers: passive targeting and crossing of biological barriers. *Curr Med Chem*. 2012;19:3070-3102.

78. Thomas OS, Weber W. Overcoming physiological barriers to nanoparticle delivery—are we there yet? *Front Bioeng Biotechnol*. 2019;7:415.

79. Ernsting MJ, Murakami M, Roy A, Li S. Factors controlling the pharmacokinetics, biodistribution and intratumoral penetration of nanoparticles. *J Control Release*. 2013;172:782-794.

80. Hauert S, Berman S, Nagpal R, Bhatia SN. A computational framework for identifying design guidelines to increase the penetration of targeted nanoparticles into tumors. *Nano Today*. 2013;8:566-576.

81. Stylianopoulos T, Economides E, Baish JW, Fukumura D, Jain RK. Towards optimal design of cancer nanomedicines: multi-stage nanoparticles for the treatment of solid tumors. *Ann Biomed Eng*. 2015;43:2291-2300.

82. Stylianopoulos T, Soteriou K, Fukumura D, Jain RK. Cationic nanoparticles have superior transvascular flux into solid tumors: insights from a mathematical model. *Ann Biomed Eng*. 2013;41:68-77.

83. Dai Q, Wilhelm S, Ding D, et al. Quantifying the ligand-coated nanoparticle delivery to cancer cells in solid tumors. *ACS Nano*. 2018;12:8423-8435.

84. Priwitaningrum DL, Blonde JG, Sridhar A, et al. Tumor stroma-containing 3D spheroid arrays: a tool to study nanoparticle penetration. *J Control Release*. 2016;244:257-268.

85. Vonarbourg A, Passirani C, Saulnier P, Benoit J. Parameters influencing the stealthiness of colloidal drug delivery systems. *Biomaterials*. 2006;27:4356-4373.

86. Sakai-Kato K, Yoshida K, Izutsu K. Effect of surface charge on the size-dependent cellular internalization of liposomes. *Chem Phys Lipids*. 2019;224:104726.

87. Zou Y, Ito S, Yoshino F, Suzuki Y, Zhao L, Komatsu N. Polyglycerol grafting shields nanoparticles from protein Corona formation to avoid macrophage uptake. *ACS Nano*. 2020;14:7216-7226.

88. Jiang W, Lionberger R, Yu LX. In vitro and in vivo characterizations of PEGylated liposomal doxorubicin. *Bioanalysis*. 2011;3:333-344.

89. Vaage J, Barberaguillem E, Abra R, Huang A, Working P. Tissue distribution and therapeutic effect of intravenous free or encapsulated liposomal doxorubicin on human prostate carcinoma xenografts. *Cancer*. 1994;73:1478-1484.

90. Ogawara K, Un K, Minato K, Tanaka K, Higaki K, Kimura T. Determinants for in vivo anti-tumor effects of PEG liposomal doxorubicin: importance of vascular permeability within tumors. *Int J Pharm*. 2008;359:234-240.

91. Gabizon A, Martin F. Polyethylene glycol coated (pegylated) liposomal doxorubicin - rationale for use in solid tumours. *Drugs*. 1997;54: 15-21.

92. del Pino P, Yang F, Pelaz B, et al. Basic physicochemical properties of polyethylene glycol coated gold nanoparticles that determine their interaction with cells. *Angew Chem Int Ed*. 2016;55:5483-5487.

93. Shen Z, Ye H, Kroeger M, Li Y. Aggregation of polyethylene glycol polymers suppresses receptor-mediated endocytosis of PEGylated liposomes. *Nanoscale*. 2018;10:4545-4560.

94. Kurtz-Chalot A, Villiers C, Pourchez J, et al. Impact of silica nanoparticle surface chemistry on protein corona formation and consequential interactions with biological cells. *Mater Sci Eng C: Mater Biol Appl*. 2017;75:16-24.

95. Li Y, Hu Y. Computational investigation of the influence of chain length on the shielding effect of PEGylated nanoparticles. *RSC Adv*. 2014;4:51022-51031.

96. Labouta HI, Gomez-Garcia MJ, Sarsons CD, et al. Surface-grafted polyethylene glycol conformation impacts the transport of PEG-functionalized liposomes through a tumour extracellular matrix model. *RSC Adv*. 2018;8:7697-7708.

97. Tang Y, Wang X, Li J, et al. Overcoming the reticuloendothelial system barrier to drug delivery with a "don't-eat-us" strategy. *ACS Nano*. 2019;13:13015-13026.

98. Hama S, Itakura S, Nakai M, et al. Overcoming the polyethylene glycol dilemma via pathological environment-sensitive change of the surface property of nanoparticles for cellular entry. *J Control Release*. 2015;206:67-74.

99. Gyenge EB, Darphin X, Wirth A, et al. Uptake and fate of surface modified silica nanoparticles in head and neck squamous cell carcinoma. *J Nanobiotechnol*. 2011;9:32.

100. Bachir ZA, Huang Y, He M, et al. Effects of PEG surface density and chain length on the pharmacokinetics and biodistribution of methotrexate-loaded chitosan nanoparticles. *Int J Nanomed*. 2018;13:5657-5671.

101. Gaumet M, Vargas A, Gurny R, Delie F. Nanoparticles for drug delivery: the need for precision in reporting particle size parameters. *Eur J Pharm Biopharm*. 2008;69:1-9.

102. Sindhwani S, Syed AM, Ngai J, et al. The entry of nanoparticles into solid tumours. *Nat Mater*. 2020;19:566-575.

103. Cattaneo L, Zunino P. A computational model of drug delivery through microcirculation to compare different tumor treatments. *Int J Numer Methods Biomed Eng*. 2014;30:1347-1371.

104. Shipley RJ, Sweeney PW, Chapman SJ, Roose T. A four-compartment multiscale model of fluid and drug distribution in vascular tumours. *Int J Numer Methods Biomed Eng*. 2020;36:e3315.

105. Liu JF, Jang B, Issadore D, Tsourkas A. Use of magnetic fields and nanoparticles to trigger drug release and improve tumor targeting. *Wiley Interdiscip Rev: Nanomed Nanobiotechnol*. 2019;11:e1571.

106. Wang Y, Leng S, Huang J, Shu M, Papavassiliou DV. Modeling of cancer photothermal therapy using near-infrared radiation and functionalized graphene nanosheets. *Int J Numer Methods Biomed Eng*. 2020;36:e3275.

107. Cho EC, Xie J, Wurm PA, Xia Y. Understanding the role of surface charges in cellular adsorption versus internalization by selectively removing gold nanoparticles on the cell surface with a I-2/KI etchant. *Nano Lett*. 2009;9:1080-1084.

SUPPORTING INFORMATION

Additional supporting information may be found online in the Supporting Information section at the end of this article.